

Artificial Relativistic Molecules

Jae Whan Park^{1,†}, Hyo Sung Kim^{1,2,†}, Thomas Brumme³, Thomas Heine^{3,4,5}, and Han Woong Yeom^{1,2*}

¹Center for Artificial Low Dimensional Electronic Systems,

Institute for Basic Science (IBS), 77 Cheongam-Ro, Pohang 790-7884, Korea.

²Department of Physics, Pohang University of Science and Technology, Pohang 790-784, Korea

³Department of Chemistry, University of Leipzig, Leipzig Germany

⁴School of Science, Faculty of Chemistry and Food Chemistry, TU Dresden, 01062 Dresden, Germany and

⁵Institute of Resource Ecology, Helmholtz Center Dresden-Rossendorf, Leipzig Research Branch, Permoserstr. 15, 04318 Leipzig, Germany

Abstract

We fabricate artificial molecules composed of heavy atom lead on a van der Waals crystal. Pb atoms templated on a honeycomb charge-order superstructure of IrTe₂ form clusters ranging from dimers to heptamers including benzene-shaped ring hexamers. Tunneling spectroscopy and electronic structure calculations reveal the formation of unusual relativistic molecular orbitals within the clusters. The spin-orbit coupling is essential both in forming such Dirac electronic states and stabilizing the artificial molecules by reducing the adatom-substrate interaction. Lead atoms are found to be ideally suited for a maximized relativistic effect. This work initiates the use of novel two dimensional orderings to guide the fabrication of artificial molecules of unprecedented properties.

Introduction

Artificial atomic clusters or lattices supported on solid surfaces can exhibit tailored electronic, magnetic, and topological properties of fundamental and technological importance. For example, atomic-scale chains and clusters disclosed the quantum confinement of electrons [1–6], topological edge modes [7], superlattice Dirac bands [8], flat bands [9], atomic scale spin interactions [10], and topological defects [11, 12]. The direct atom-by-atom manipulation and the self-assembly of atoms or molecules are two major approaches to realize such atomic scale chains, clusters, and finite lattices. Both methods, however, have their own limitations under given interatomic interactions and fabricating energetically and kinetically unfavorable structures or assemblies has been a huge challenge [13].

In case of the self assembly of supported clusters, such limitations may be overcome by templates, which provide unusual growth environments to produce otherwise unfavored molecular structures. Step edges and one-dimensional surface superstructures were actively used as such templates on metal [14–16] and Si surfaces [17]. The growth of metal atoms on these substrates leads to unusually anisotropic clusters. On the other hand, nano-sized two dimensional superstructures were suggested as novel templates, such as the moiré structure of hexagonal boron nitride [18, 19], metal-organic frameworks of DNA [20, 21], and metal-organic honeycomb networks on metal surfaces [22–25]. However, while the confinement of metal atoms and molecules on these templates were demonstrated, the formation of artificial molecules was not reported yet.

In this work we employ a novel template-guided atomic self-assembly technique and take advantage of the strong relativistic effects in lead atoms that effectively create long-ranged interatomic bonds. This allows us to produce a series of unprecedented artificial molecules with relativistic, so called Dirac, electronic orbitals. The honeycomb charge-order superstructure of the van der Waals (vdW) crystal IrTe₂ [26] cages various Pb clusters ranging from dimers to heptamers including those in interesting benzene-like hexagonal rings. Atomically-resolved spectroscopy and electronic structure calculations reveal clearly the formation of molecular orbitals by direct orbital overlap between neighboring Pb adatoms. The spin-orbit coupling (SOC) of Pb atoms and of the substrate is shown to enhance the interatomic interaction to drive the formation of unprecedentedly relativistic molecules at an unusually large interatomic distance. This case exemplifies the chemical stabilization of nanoscale assemblies uniquely by relativistic effects and opens the potential of novel superstructures on vdW crystals for the fabrication of otherwise unfavored molecules with unprecedented properties.

Results

Charge order superstructure hosts Pb clusters

Figure 1a shows Pb adatoms deposited on the honeycomb charge-order superstructure at the surface of a IrTe₂ vdW crystal. Below 180 K, a honeycomb superstructure forms with a period of 2.2 nm by the spontaneous ordering of 5d³⁺ and 5d⁴⁺ valence electrons of Ir (with the buckling of the Te layer accompanied) and competes with various stripe charge orders [26]. Pb adatoms sit at hollow sites surrounded by three Te atoms (Fig. 1b and Supplementary Fig. 2) and, very selectively with yet unclear

*Electronic address: yeom@postech.ac.kr

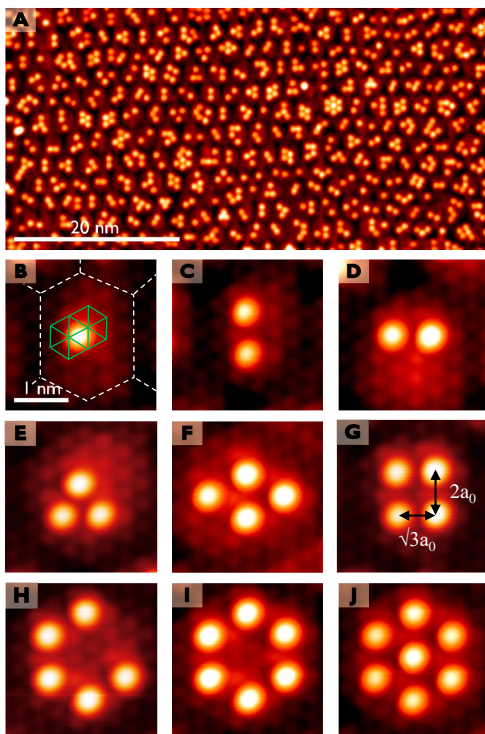


Figure 1: STM topography of Pb clusters on IrTe₂. **a** A typical IrTe₂ surface decorated with Pb adatoms in the hexagonal charge order state ($V_s = 1.5$ V, $I_t = 0.05$ nA). Scale bar, 20 nm. **b-j** Various Pb clusters are observed on a single hexagon ($V_s = 20$ mV, $I_t = 1$ nA): **b** Monomer (Scale bar, 1 nm), **c** $2a_0$ -spaced dimer, **d** $\sqrt{3}a_0$ -spaced dimer, **e** $\sqrt{3}a_0$ -spaced trimer, **f** $2a_0$ -spaced tetramer, **g** mixed spacing tetramer, **h** $2a_0$ -spaced pentamer, **i** $2a_0$ -spaced hexamer, and **j** $2a_0$ -spaced heptamer. Green solid lines and white dashed lines in **b** denote the Te-(1×1) lattice and the charge-order hexagon lattice, respectively.

reasons, inside of each honeycomb, which are above Ir atoms with the $5d^{4+}$ valency (see Supplementary Fig. 1). Density-functional theory (DFT) calculations including SOC consistently predict the four-fold hollow site adsorption with an adsorption energy of -1.93 eV against the three-fold hollow site of -1.74 eV and Te on-top site of -1.16 eV. Clusters ranging from one to seven Pb atoms are confined within a honeycomb unitcell with various lateral configurations. The Pb-Pb interatomic distance is dictated by the substrate with two choices of $\sqrt{3}a_0$ or $2a_0$ (a_0 , the IrTe₂ lattice constant of 3.5 Å [26]). The $2a_0$ -spaced dimers (Fig. 1c) are more frequently observed than those of $\sqrt{3}a_0$ Pb-Pb distance (Fig. 1d). As trimers, a heterogeneous trimer with a Pb-Pb spacing both of $\sqrt{3}a_0$ and $2a_0$ or a compact one of $2a_0$ or $\sqrt{3}a_0$ are formed (Fig. 1e and Supplementary Fig. 4c). Figures 1f and 1g show a tetramer formed by two $2a_0$ dimers and one with $\sqrt{3}a_0$ and $2a_0$ dimers, respectively. We also find benzene-like hexagonal ring clusters as shown in Figs. 1h, 1i, and 1j among a few other interesting clusters. These configurations are made only by $2a_0$ building blocks and are the

largest clusters confined within the hexagonal unit of the template.

Relativistic molecular orbitals in Pb dimers

Electronic energy levels of Pb clusters are revealed by scanning tunneling spectroscopy (STS). For a monomer (Fig. 2c), we observe three main spectral features at 1.40, 1.71, and 1.93 eV for Pb $6p$ valence electrons. Our calculation shows that a Pb adatom is partly ionized by donating $6p$ electrons into the substrate to shift the $6p$ states to unoccupied states (Fig. 2o and Fig. 2w). As shown in Fig. 2w, the relativistic effect of SOC splits the $6p$ states into $6p_{1/2}$ and $6p_{3/2}$ Dirac orbitals and the latter splits further due to the substrate-induced splitting of in-plane (p_{xy}) and out-of-plane (p_z) orbitals. Consequently, three main peaks correspond to the relativistic p orbitals of $p_{1/2}$ ($j=1/2$, $m_j = \pm 1/2$) and $p_{3/2}$ ($j=3/2$, $m_j = \pm 3/2, \pm 1/2$), respectively.

In case of a dimer with a shorter Pb-Pb distance, an energy splitting (0.23 eV) of molecular bonding and antibonding states is observed clearly for the $6p_{1/2}$ state (Fig. 2j). In a longer dimer, the splitting is much smaller, about 0.10 eV, as the orbital overlap reduces (Fig. 2f). Our DFT calculation predicts (Figs. 2r and 2v) the lowest molecular orbital splittings of 0.05 and 0.18 eV for the longer and shorter dimers, respectively, in reasonable agreement with the experiment. The present DFT calculation seems to underestimate the molecular bonding interaction by about 0.05 eV. These energy scale is consistent with what are expected for a freestanding Pb-Pb dimer (Supplementary Fig. 6). This result clearly indicates the molecular orbital formation within the Pb clusters at an unusually large Pb-Pb distance of 7 Å, which is observed consistently for all cluster configurations identified (Supplementary Fig. 7).

The molecular levels of a Pb dimer are well explained by the simple tight-binding interaction of Dirac atomic orbitals [27] perturbed weakly by the substrate as discussed above. That is, three relativistic p orbitals split simply into the combination of molecular orbitals in gerade (g) and ungerade (u) symmetries (see Fig. 2w). For example, the two lowest peaks correspond to the combination of the $p_{1/2}$ orbitals in g and u symmetries. The resulting Dirac molecular orbitals are clearly differentiated from their scalar-relativistic counterparts of σ and π molecular orbitals. The g (u) orbital consists of one-third σ -bond (σ -antibond) and two-third π -antibond (π -bond) character, indicating a substantial mixing between σ - and π -bonds due to the full relativity effect of SOC. The Dirac basis and the interaction with substrate atoms also breaks the mirror symmetry perpendicular to the dimer axis. This is reasonably confirmed in the experiment (Figs. 2h and 2i) and in the calculation (Figs. 2t and 2u). Further details of the interaction with the substrate will be discussed below, which become important for the understanding of the relativistic effect on the adsorption energy.

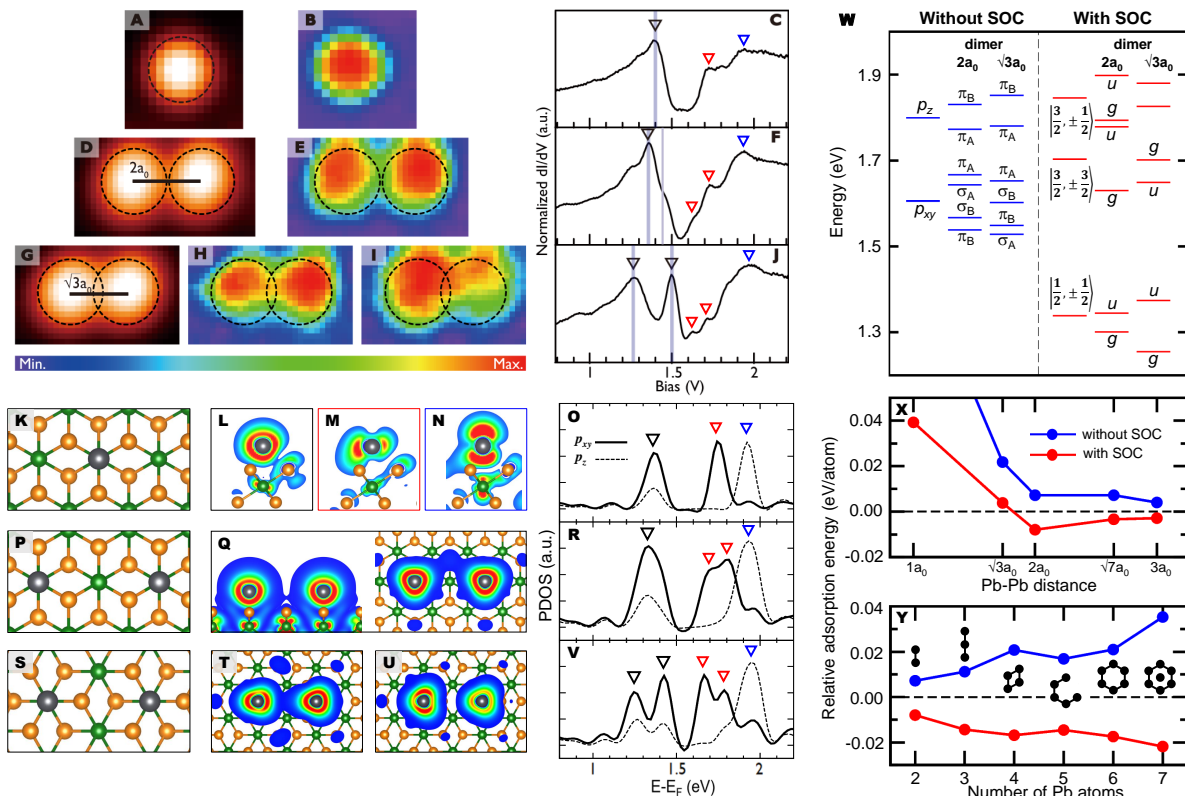


Figure 2: Relativistic effects for the Pb monomer and dimers on IrTe₂. a, d, g STM topography images, b, e, h, i dI/dV maps, and c, f, j STS spectra for a Pb monomer, a $2a_0$ -spaced dimer, and a $\sqrt{3}a_0$ spaced dimer, respectively. The dI/dV maps were obtained at the peak positions of STS spectra marked by the inverted black triangles. The corresponding theoretical results are presented in k-v. k, p, s atomic structures, l-n, q, t, u charge density plots, and o, r, v projected density of states (DOS) for a Pb monomer on the IrTe₂- (5×5) supercell, a $2a_0$ -spaced dimer, and a $\sqrt{3}a_0$ -spaced dimer, respectively. Gray, orange, and green balls in atomic structures represent Pb, Te, and Ir atoms, respectively. Charge densities were obtained for the peak energies of the DOS, three peaks for a monomer, the lowest-energy peak (top and side view) for a $2a_0$ -spaced dimer, and the two lowest-energy peaks for a $\sqrt{3}a_0$ -spaced dimer. w DFT energy level at Γ point of a Pb monomer and dimers on IrTe₂- (5×5) without and with spin-orbit coupling. For better comparison with experiments, the Fermi level of the Pb/IrTe₂ surface is shifted down by 0.7 eV. Relative adsorption energy per Pb atom of x a Pb dimer on IrTe₂- (7×7) as a function of Pb-Pb distance and y various Pb molecules with a Pb-Pb distance of $2a_0$. The adsorption energy of isolated Pb atom set to zero. Blue and red data denote the cases without and with spin-orbit coupling, respectively.

The direct and real space observation of relativistic molecular orbitals is exceptional, since most of previous experiments for very few heavy element molecules relied on spectroscopy techniques [28–31] and, thus, the relativistic effects were mainly discussed in theoretical aspects [32, 33]. Although a Pb dimer has a much longer bond length (7 Å) than other relativistic molecules [33–35] and there is a substantial adatom-substrate interaction, the molecular splitting mainly arises from the direct overlap of relativistic p orbitals. This is distinguished from the substrate-mediated long-range interaction of other metal clusters on metal surfaces [36, 37].

Mechanism of the interaction between Pb atoms

It is important to point out that the attractive interaction between Pb adatoms is only due to SOC and that the $2a_0$ distance imposed by the substrate is optimal for

the formation of a Pb dimer (Fig. 2x) in our calculations. This is consistent with the observation of the higher population of $2a_0$ dimers. The SOC energetics for the larger Pb molecules, from trimer to heptamer (Fig. 2y and Supplementary Fig. 10), is also consistent with the experimental observation of larger Pb molecules with exclusively $2a_0$ nearest-neighbor distance. The $2a_0$ distance is optimized by two competing energy contributions, the ionic (or dipole) repulsion and the orbital overlap energy gain of adatom-substrate hybridized states. The comparison of the calculated differential charges with and without SOC reveals two sophisticated SOC effects for those contributions; (i) a reduced donation of p electrons to the substrate to reduce the ionic repulsion and (ii) an enhanced orbital overlap of the Pb-Te hybridized states (see Supplementary Fig. 10). The former is due to the lowering of the atomic energy level of Dirac orbitals by SOC. It is also partly due to the charge redistribution of

the IrTe₂ substrate by SOC, namely the charge transfer from the d_{z^2} states of Ir atom to Te atoms. The substantial interaction of Pb with the substrate Te orbitals provides an extra energy gain for the antibonding level of the $p_{1/2}$ ($m_j = \pm 3/2$) orbital of the $\sqrt{3}a_0$ dimer (see Supplementary FIG. 9b). That is, the intertwined effect of the substrate and the relativity determines the stability of the Pb molecules. In these respects, Pb is ideal since it has very strong relativistic effects (in comparison, for example, to Sn, see Supplementary Fig. 11) and a proper interaction strength with the substrate (in comparison to Tl, see Supplementary Fig. 12). Of course, the formation of Pb molecules would also be affected by the size and shape of the charge-order honeycomb template.

Benzene-like ring-shaped Dirac molecules While a consistent interaction mechanism holds for all 15 different Pb molecules identified (Supplementary Fig. 4), particularly interesting ones are those based on a six-fold hexagonal ring (Fig. 3). The benzene-like ring molecule of Pb₆ with a $2a_0$ Pb-Pb distance exhibit the weak molecular splitting similar to a $2a_0$ dimer (Fig. 3e). The intriguing molecular orbital formation is clearly imaged by the dI/dV maps: (i) the broken AB sublattice symmetry for the lowest energy state (Fig. 3b), (ii) a Kekulé-like distortion for the second state (Fig. 3c), and (iii) a mirror-symmetry-broken two-fold-symmetric bonding feature for the third state (Fig. 3d). Our calculation reproduces well the spatial characteristics of these molecular orbitals, which are indeed due to the relativistic character and the interaction with the substrate (Fig. 3l-n and Supplementary Fig.13). Note, however, the remaining energetic discrepancy between experiment and calculation. The present calculations underestimate the molecular bonding interaction and the calculated spectral features are almost degenerate at around 1.3 eV for the benzene-like molecule. We think that this difference is at least partly due to the limitation of our model in taking into account of the substrate electronic states in its charge-ordered correlated state [26]. Another interesting molecule is the Pb pentamer (Figs. 3f-3j), whose Dirac molecular orbitals are also reasonably well simulated (Figs. 3p-3t). Such type of an individual open ring molecule cannot be synthesized. The Pb₅ molecule features the edge states at both truncated ends between the bonding and antibonding levels of three Dirac p orbitals (see Supplementary Fig. 14). It indicates the ring-type Pb molecules are circularly delocalized electron systems. The formation of a filled-benzene-ring molecule is also highly unusual (Fig. 1j), where the interatomic overlap is much enhanced by the central Pb atom with unique bonding configurations (Supplementary Figs.15-17). This molecule can be compared with a rare example of a planar B₇ molecule [38] except for the strong SOC. While not accessible by the present experiments, the benzene-type Dirac molecular orbitals fabricated here have unique and interesting spin configurations (see Sup-

plementary Fig. 13), which may be exploited further. It becomes very obvious that the present artificial Pb molecules introduce unprecedented molecular configurations combined with the strong SOC.

Summary We fabricate various artificial Pb molecules utilizing a novel honeycomb template of the charge-ordered superstructure in IrTe₂. The molecular orbital formation is clearly observed in the Pb clusters from dimers to unusual benzene-ring-type molecules. The spin-orbit coupling is found to play crucial roles in both the condensation of Pb atoms and the molecular orbital formation, bringing them into an unprecedented regime of relativistic Dirac molecules. Beyond the relativistic chemistry, the unusual bonding and spin structure of these relativistic molecular orbitals may be combined with the novel electronic properties of the substrate such as the charge ordering and the emerging superconductivity [26] to lead to a new type of a quantum system. In addition to the versatile technique of atom-by-atom manipulation, where the interatomic distance may be varied, the use of various types of 2D superstructures as templates would definitely extend the potential of molecular or cluster self assemblies. Interesting 2D superstructures can include twisted bilayer graphene [39] and domain-wall or twin-boundary networks of transition metal dichalcogenides [40, 41]. The templated self assembly of magnetic atoms on such substrates can be very interesting due to the proximity to the novel 2D electronic states of substrates.

Methods

Sample preparation Single crystals of IrTe₂ were grown by Te flux using pre-sintered IrTe₂ polycrystals as reported previously. Samples were cleaved in a vacuum better than 5×10^{-10} torr at room temperature. Pb atoms are grown on cleaved IrTe₂ surfaces at room temperature. The Pb atom tends to cover the IrTe₂ surface up to 0.1 ML. Over this coverage, this Pb growth mode depends on the deposition temperature. For example, when the Pb grows at room temperature, Pb forms a uniform film. However, at low temperature deposition, depending on the coverage and annealing condition, we can found different heights of the Pb islands.

STM measurement All the STM measurements were performed with a commercial ultrahigh vacuum cryogenic STM (Specs, Germany) in the constant-current mode with PtIr tips at 4.3 K. The differential conductance, dI/dV , was measured using the lock-in detection with a modulation of 1.17 kHz.

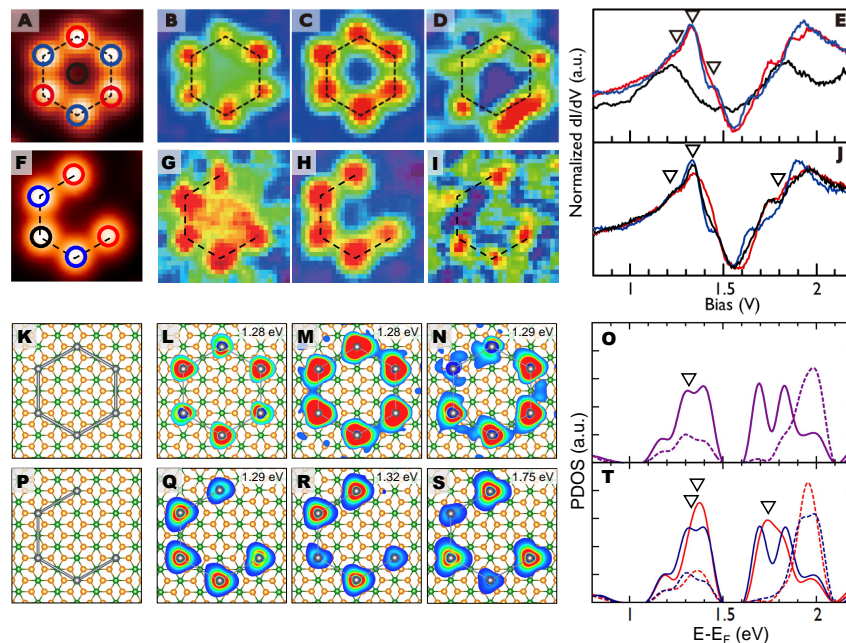


Figure 3: Benzene-ring-shaped Pb clusters on IrTe₂. **a, f** STM topography, **b-d, g-i** dI/dV maps, and **e, j** STS spectra for a Pb hexamer and a pentamer, respectively. dI/dV maps are taken at the energies indicated in the STS spectra. Red, blue and black lines in the STS spectra are obtained at the red, blue, and black Pb atoms indicated in **a** and **f**. The corresponding theoretical results are presented in **k-t**. **k, p** atomic structure, **l-n, q-s** charge densities at the given energies (spin decoupled and spin summed, respectively), and **o** and **t** projected DOS, for a Pb hexamer and a pentamer on IrTe₂-(7×7), respectively. For the Pb hexamer, the localized DOS at red and blue Pb atoms is identical to each other. For the Pb pentamer, the red (dark-blue) line denote the localized states at truncated end atoms (the other Pb atoms). Solid and dashed lines represent p_{xy} and p_z states, respectively.

DFT calculations We perform the relativistic DFT calculations using the Vienna *ab initio* simulation package [42] within the generalized gradient approximation of the Perdew-Burke-Ernerhof type [43] and the projector augmented-wave method [44]. The IrTe₂ surface is modeled by a (5×5) and (7×7) supercell with a single IrTe₂ layer and a vacuum spacing of about 23.6 Å. The calculated value 3.839 Å is used as the lattice constant of IrTe₂. We use a plane-wave basis with a cutoff of 211 eV for expansion of electronic wave functions and a 15×15×1 k -point mesh for the 1×1 Brillouin-zone integrations. To avoid the unexpected substrate distortion of the IrTe₂,

only adsorbed Pb atoms are relaxed until the residual force components are within 0.02 eV/Å. Here the Fermi level was shifted down by 0.70 eV because to overcome the inherent discrepancy between experiment and theory due to unknown charge-ordered structure, doping effect of the Pb adsorbates and the IrTe₂ sample and/or the inaccuracy of DFT band-energy calculations.

Data availability The authors declare that the data supporting the findings of this study are available within the article and its Supplementary Information.

-
- [1] Nilius, N., Wallis, T. M. & Ho. W. Development of one-dimensional band structure in artificial gold chains. *Science* **297**, 1853 (2002).
- [2] Nilius, N., Wallis, T. M., Person, M. & Ho. W. Distance dependence of the interaction between single atoms: Gold dimers on NiAl(110). *Phys. Rev. Lett.* **90**, 196103 (2003).
- [3] Fölsch, S., Hyldgaard, P., Koch, R & Ploog, K. H. Quantum confinement in monatomic Cu chains on Cu(111). *Phys. Rev. Lett.* **92**, 56803 (2004).
- [4] Wallis, T. M., Nilius, N., Mokaelian, G., & Ho. W. Electronic properties of artificial Au chains with individual Pd impurities. *J. Chem. Phys.* **122**, 011101 (2005).
- [5] Lagoute, J., Liu, X. & Fölsch, S. Link between adatom resonances and the Cu(111) shockley surface state. *Phys. Rev. Lett.* **95**, 136801 (2005).
- [6] Stroschio, J. A. *et al.* Electronically induced atom motion in engineered CoCu_n nanostructures. *Science* **313**, 948 (2006).
- [7] Nadj-Perge, S. *et al.* Observation of Majorana fermions in ferromagnetic atomic chains on a superconductor. *Science* **346**, 602 (2014).
- [8] Yankowitz, M. *et al.* Emergence of superlattice Dirac points in graphene on hexagonal boron nitride.

- Nat. Phys.* **8**, 382 (2012).
- [9] Slot, M. R. *et al.* Experimental realization and characterization of an electronic Lieb lattice. *Nat. Phys.* **13**, 372 (2017).
- [10] Hirjibehedin, C. F., Christopher, P. L., & Heinrich, A. J. Spin coupling in engineered atomic structures. *Science* **312**, 1021 (2006).
- [11] Cheon, S., Kim, T.-H., Lee, S.-H., & Yeom, H. W. Chiral solitons in a coupled double Peierls chain. *Science* **350**, 182 (2015).
- [12] Drost, R., Ojanen, T., Harju, A. & Liljeroth, P. Topological states in engineered atomic lattices. *Nat. Phys.* **13**, 668 (2017).
- [13] Chichak, K. S. *et al.* Molecular Borromean rings. *Science* **304**, 1308 (2004).
- [14] Lobo, J. *et al.* Tuning the surface state dimensionality of Cu nanostripes. *Phys. Rev. Lett.* **93**, 137602 (2004).
- [15] Hermes, S., Schröder, F., Chelmowski, R., Wöll, C. & Fischer, R. A. Selective nucleation and growth of metal-organic open framework thin films on patterned COOH/CF₃- terminated self-assembled monolayers on Au(111). *J. Am. Chem. Soc.* **127**, 13744 (2005).
- [16] Barth, J. V., Costantini, G. & Kern, K. Engineering atomic and molecular nanostructures at surface. *Nature* **437**, 671 (2005).
- [17] Kang, P.-G., Jeong, H., & Yeom, H. W., Microscopic mechanism of templated self-assembly: Indium metallic atomic wires on Si(553)-Au. *Phys. Rev. B* **79**, 113403 (2009).
- [18] Corso, M. *et al.* Boron nitride nanomesh. *Science* **303**, 217 (2004).
- [19] Dil, H. *et al.* Surface trapping of atoms and molecules with dipole rings. *Science* **319**, 1824 (2008).
- [20] LaBean, T. H. *et al.* DNA-Templated self-assembly of protein arrays and highly conductive nanowires. *Science* **301**, 5641 (2003).
- [21] Kiehl, R. A. *et al.* DNA-Templated self-assembly of metallic nanocomponent arrays on a surface. *Nano Lett.* **4**, 2343 (2004).
- [22] Cheng, Z. *et al.* Adsorbates in a box: titration of substrate electronic states. *Phys. Rev. Lett.* **105**, 066104 (2010).
- [23] Pivetta, M. *et al.* Formation of Fe cluster superlattice in a metal-organic quantum-box network. *Phys. Rev. Lett.* **110**, 086102 (2013).
- [24] Nowakowska, S. *et al.* Interplay of weak interactions in the atom-by-atom condensation of xenon with in quantum boxes. *Nat. Commun.* **6**, 7342 (2015).
- [25] Müller, K., Enache, M., & Stöhr, M. Confinement properties of 2D porous molecular networks on metal surface. *J. Phys. Condens. Matter* **28**, 153003 (2016).
- [26] Kim, H. S. *et al.* Nanoscale superconducting honeycomb charge order in IrTe₂. *Nano Lett.* **16**, 4260 (2016).
- [27] Pitzer, K. S., Relativistic effects on chemical properties. *Acc. Chem. Res.* **12**, 271 (1979).
- [28] Azenha, E. G. *et al.*, Heavy-atom effects on metalloporphyrins and polyhalogenated porphyrins *Chem. Phys.* **280**, 177 (2002).
- [29] Tian, S. X., Kishimoto, N., & Ohno, K., Spin-orbit coupling effect and intramolecular orbital interactions: Penning ionization of CH₂BrCl, CHBrCl₂, and CH₂BrCN by collision with He*(2³S) metastable atoms. *J. Phys. Chem. A* **107**, 2137 (2003).
- [30] Dai, D. *et al.*, Analysis of the effect of spin-orbit coupling on the electronic structure and excitation spectrum of the Bi₂²⁻ anion in (K-crypt)₂Bi₂ on the basis of relativistic electronic structure calculations. *J. Phys. Chem. A* **109**, 1675 (2005).
- [31] Gans, B., Grassi, G. & Merkt, F., Spinorbit and vibronic coupling in the ionic ground state of iodoacetylene from a rotationally resolved photoelectron Spectrum. *J. Phys. Chem. A* **117**, 9353 (2012).
- [32] Iliáš, M., Kellö, & Urban, M., Relativistic effects in atomic and molecular properties. *Acta Physica Slovaca* **60**, 259 (2010).
- [33] van Lenthe, E., Snijders, J. G., & Baerends, E. J., The zero-order regular approximation for relativistic effects: The effect of spinorbit coupling in closed shell molecules. *J. Chem. Phys.* **105**, 6505 (1996).
- [34] Huda, M. N., Niranjana, M. K., Sahu, B. R., Klenman, L., Effect of spin-orbit coupling on small platinum nanoclusters. *Phys. Rev. A* **73**, 053201 (2006).
- [35] Li, W.-L., Lu, J.-B., Wang, Z.-L., Hu, H.-S., & Li, J., Relativity-induced bonding pattern change in coinage metal dimers M₂ (M = Cu, Ag, Au, Rg). *Inorg. Chem.* **57**, 5499, (2018).
- [36] Repp, J., Moresco, F., Meyer, G. & Rieder, K.-H. Substrate mediated long-range oscillatory interaction between adatom: Cu/Cu(111). *Phys. Rev. Lett.* **85**, 2981 (2000).
- [37] Knorr, N. *et al.* Long-range adsorbate interactions mediated by a two-dimensional electron gas. *Phys. Rev. B* **65**, 115420 (2002).
- [38] Alexandrova, A. N., Boldyrev, A. I., Zhai, H.-J., & Wang, L.-S., Electronic structure, isomerism, and chemical bonding in Bi₇⁻ and Bi₇. *J. Phys. Chem. A* **108**, 3509 (2004).
- [39] Mele E. J., Commensuration and interlayer coherence in twisted bilayer graphene. *Phys. Rev. B* **81**, 161405(R) (2010).
- [40] Cho D., *et al.* Nanoscale manipulation of the Mott insulating state coupled to charge order in 1T-TaS₂, *Nat. Commun.* **7**, 10453 (2016).
- [41] Ma Y., *et al.* Metallic twin grain boundaries embedded in MoSe₂ monolayers grown by molecular beam epitaxy. *ACS Nano* **11**, 5130 (2017).
- [42] Kresse, G. & Furthmüller, J. Efficient iterative schemes for *ab initio* total-energy calculations using a plane-wave basis set. *Phys. Rev. B* **54**, 11169 (1996).
- [43] Perdew, J. P., Burke, K. & Ernzerhof, M. Generalized gradient approximation made simple. *Phys. Rev. Lett.* **77**, 3865 (1996).
- [44] Blochl, P. E. Projector augmented-wave method. *Phys. Rev. B* **50**, 17953 (1994).

Acknowledgements J.W.P., H.S.K., and H.W.Y. were supported by Institute for Basic Science (Grant No. IBS-R014-D1). The IrTe₂ crystal was provided by S. W. Cheong in Rutgers University. J. Lee is appreciated for his help in data processing. T.B. and T.H. used the ZIH Dresden computational resources.

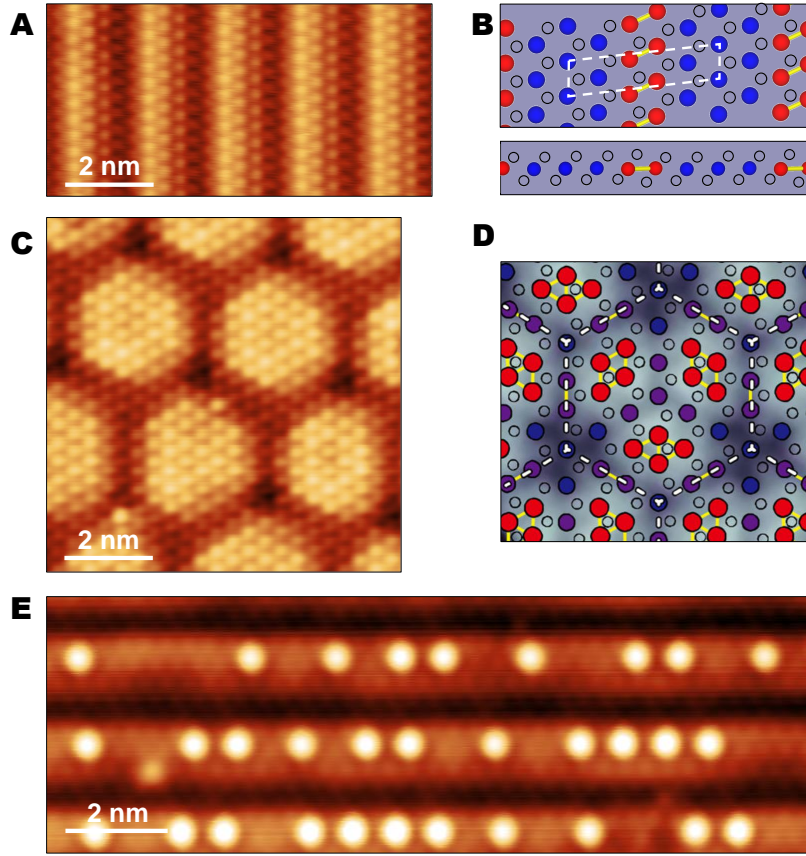
Author contributions J.W.P. performed the DFT calculations. H.S.K. carried out the STM measure-

ments. These two authors equally contributed in this paper. J.W.P. and H.W.Y. analysed the data and wrote the manuscript with the comments of all other authors. H.W.Y. supervised the research.

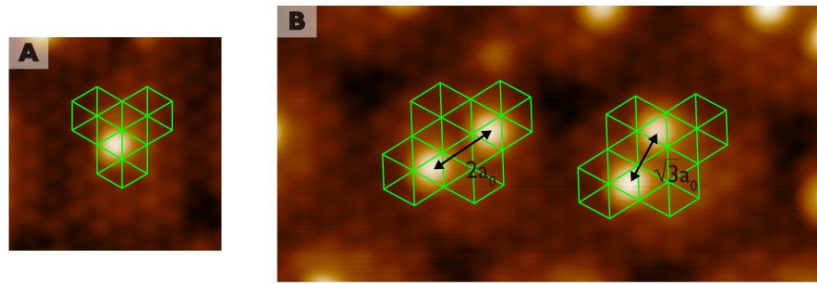
Competing interests: The authors declare no competing interests.

Supplementary Information for “Artificial Relativistic Molecules”

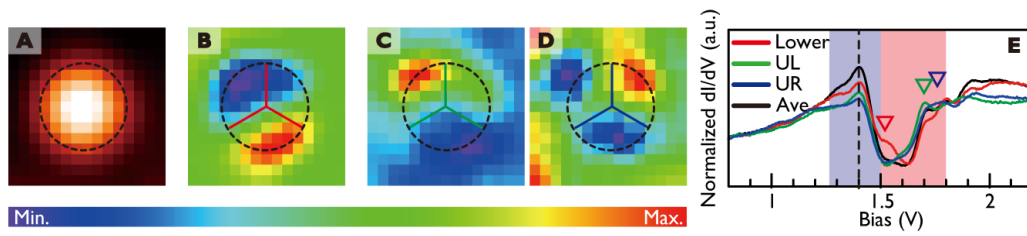
Park et al.



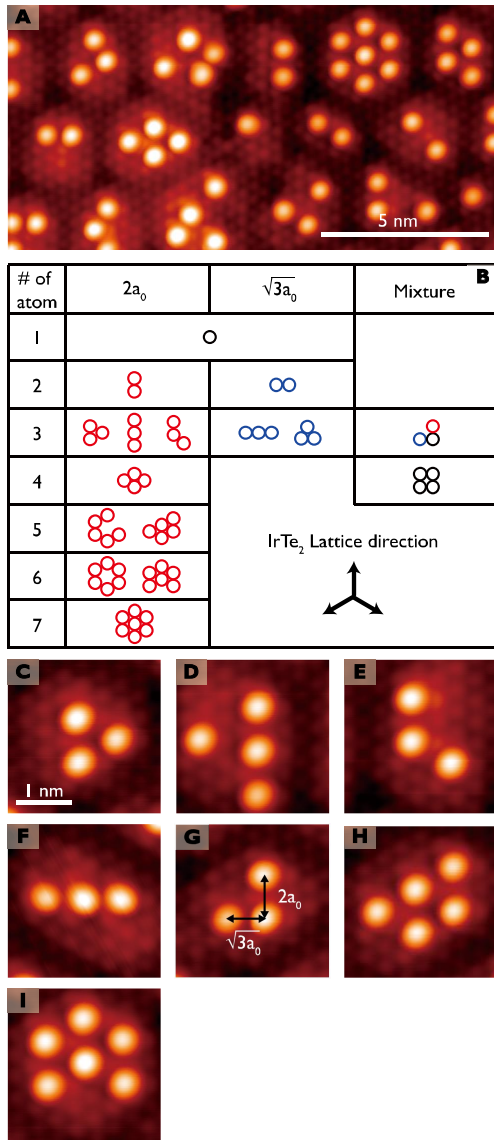
Supplementary Fig. 1: **Site selective Pb adsorption on the dimerized IrTe₂ substrate.** **a** STM image ($V_s = 5$ mV, $I_t = 1$ nA) and **b** dimerized structural model of the stripe phase (top and side views). **c** STM image ($V_s = 10$ mV, $I_t = 1$ nA) and **d** dimerized structural model of the honeycomb charge order phase. The STM topographies show the charge ordering induced by the dimerization of the Ir atoms. The dimerized Ir atoms (red circles) has $5d^{4+}$ valence electrons and others has $5d^{3+}$ valence electrons [1, 2]. **e** STM image ($V_s = 5$ mV, $I_t = 3$ nA) of the Pb atoms on the stripe phase. The Pb atoms selectively adsorb on the dimerized Ir site of the stripe phase. The atomic position of stripe phase in **b** and structural image **ind** were taken from Ref.[1] and [2], respectively.



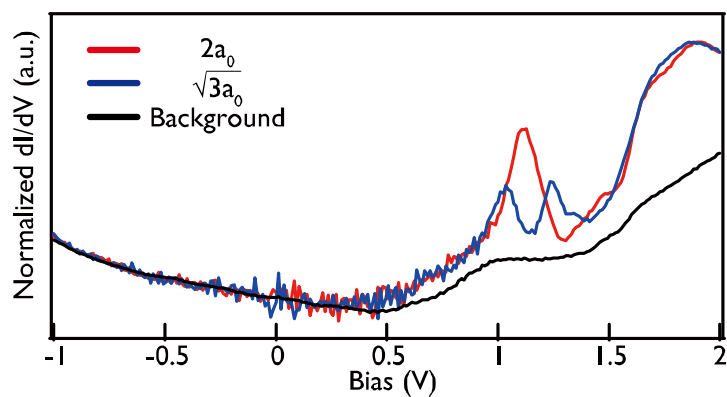
Supplementary Fig. 2: **Pb absorption site and Pb-Pb distance.** a Pb monomer and b Pb dimers. Green solid lines denote the Te-(1×1) lattice.



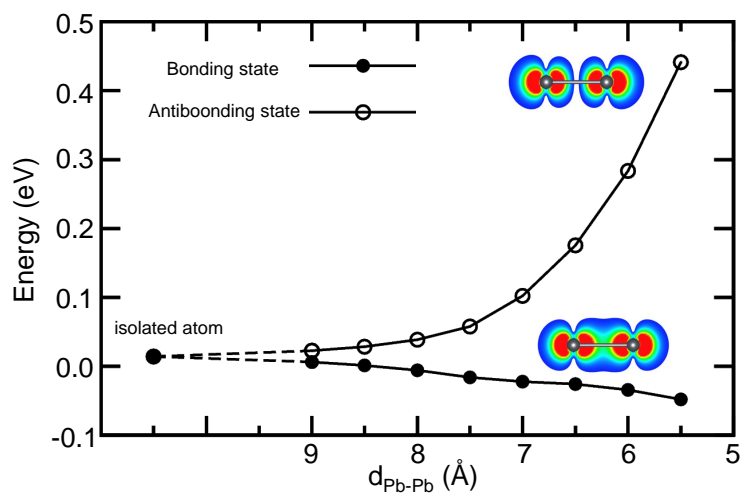
Supplementary Fig. 3: **Spatial dependence of the STS spectra.** a topography. b-d The dI/dV maps obtained at 1.52, 1.70 and 1.77 eV, respectively. e STS spectra of lower, upper left and upper right side of Pb single atom.



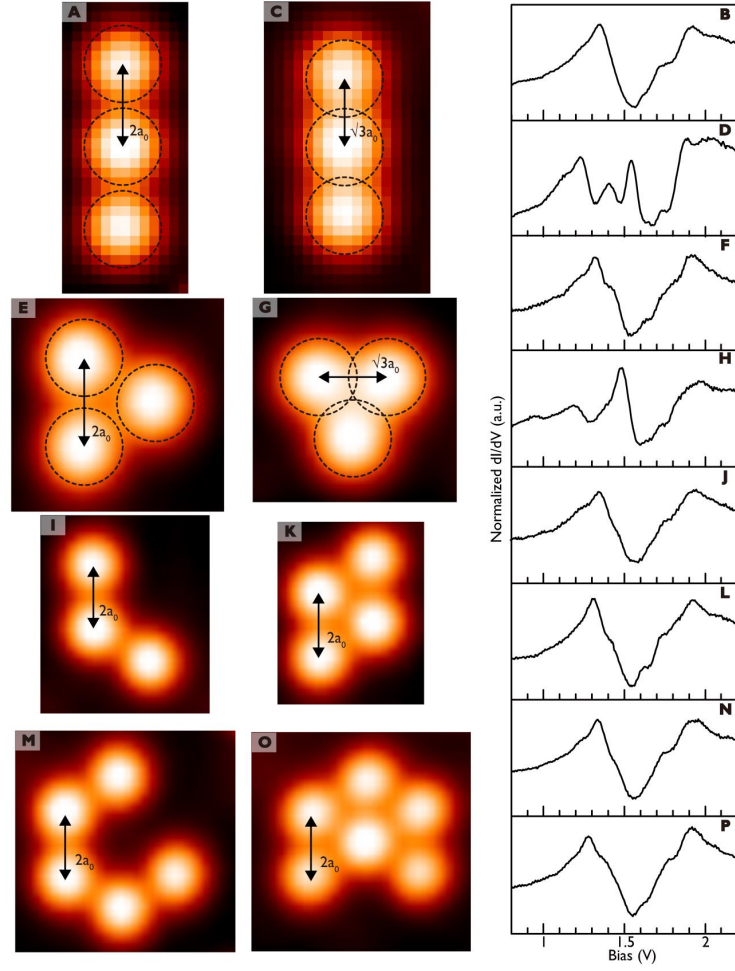
Supplementary Fig. 4: **STM topography and summary of all kinds of Pb clusters on the IrTe₂ hexagonal phase at 4.3 K.** **a** STM image of Pb clusters on atom-resolved hexagonal phase. **b** A summary of Pb clusters depending on the bonding length and the number of composed Pb atom. The IrTe₂ lattice symmetry is shown on lower right side. **c-i** Pb clusters of other configuration which is not included in Fig. 1 in text.



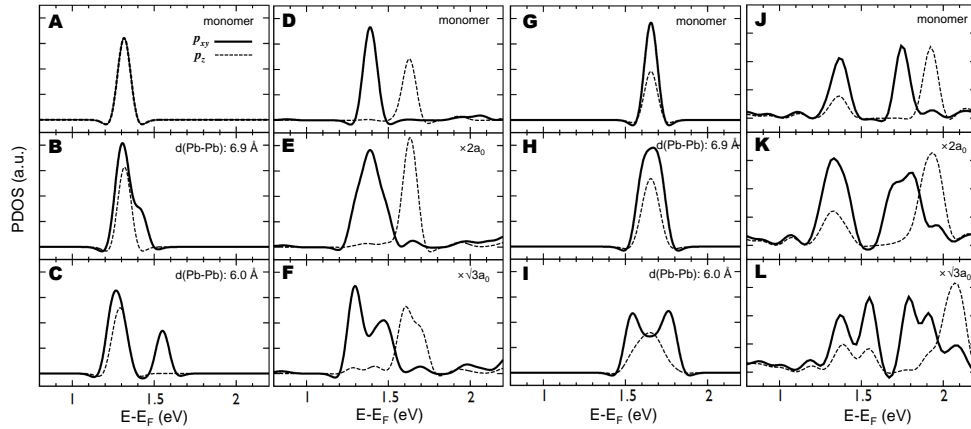
Supplementary Fig. 5: **Wide STS spectra of $2a_0$ and $\sqrt{3}a_0$ spacing Pb dimers.** Peak energy is slightly shifted with Fig. 2 in text. The energy position depends on the charge doping concentration caused by Pb coverage. Red, blue and black curves are corresponding to the $2a_0$ and $\sqrt{3}a_0$ spacing Pb dimers and background hexagons.



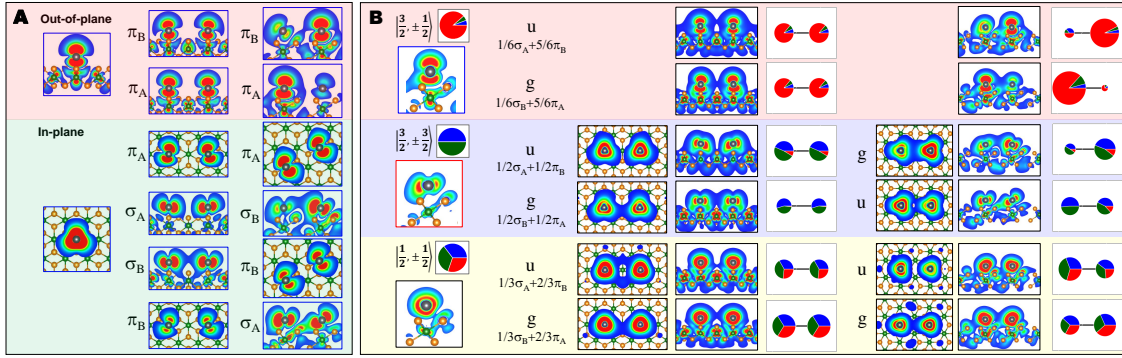
Supplementary Fig. 6: **Bonding/antibonding energy splitting of σ bond of the freestanding Pb dimer as a function of Pb-Pb distance.**



Supplementary Fig. 7: Topography and STS spectra of the Pb molecules on IrTe₂.

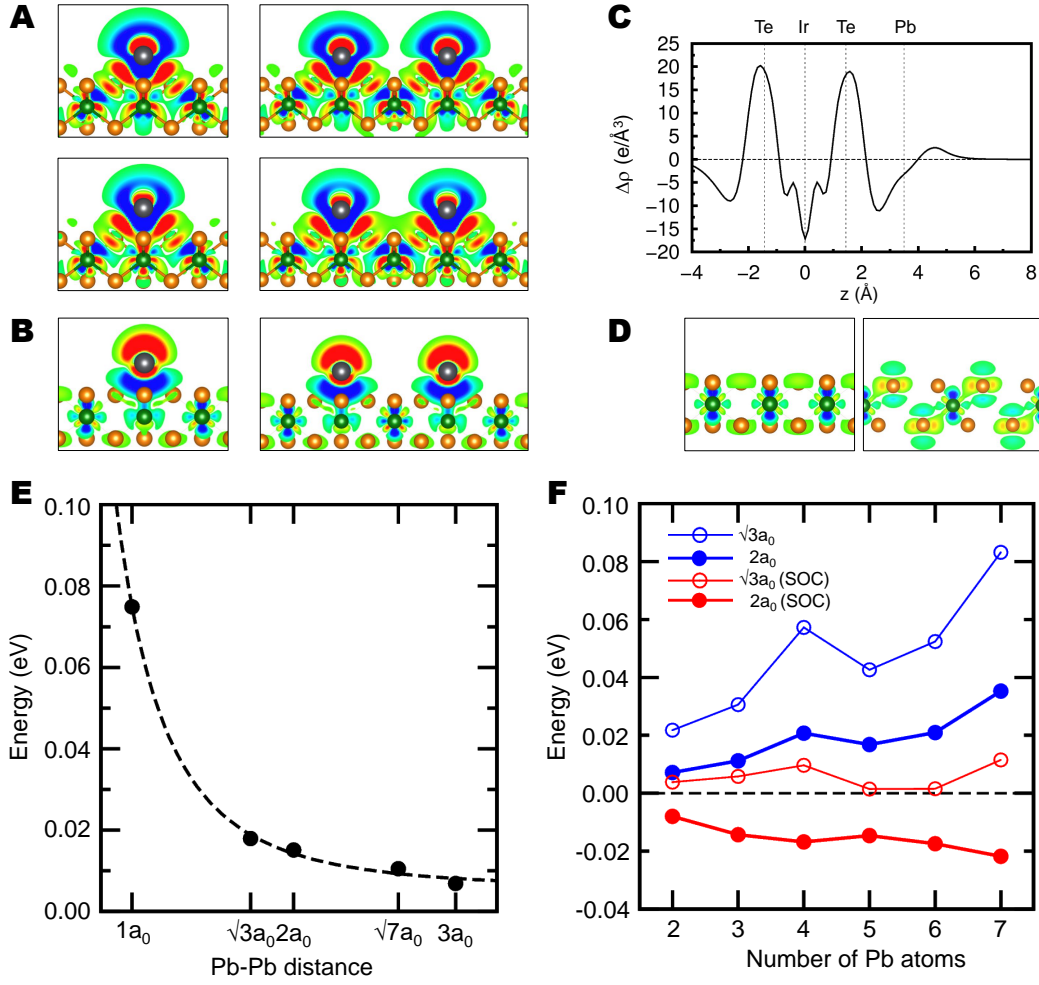


Supplementary Fig. 8: PDOS of Pb monomer and dimers. **a-c** Freestanding Pb without spin-orbit coupling (The Fermi level shifted by -1.30 eV), and **d-e** Pb on IrTe₂-(5×5) without spin-orbit coupling (The Fermi level shifted by -0.45 eV), and **a-c** Freestanding Pb with spin-orbit coupling (The Fermi level shifted by -0.45 eV), **g-i** Pb on IrTe₂-(5×5) with spin-orbit coupling (The Fermi level shifted by -0.70 eV).

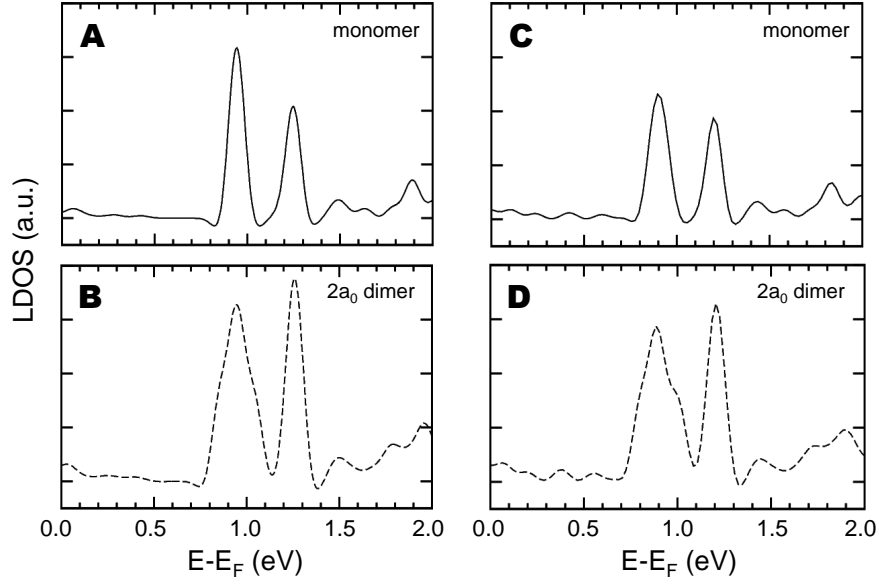


$$\begin{aligned}
 \left| \frac{1}{2}, +\frac{1}{2} \right\rangle &\propto \begin{bmatrix} -\sqrt{1/3}p_z \\ -\sqrt{1/3}(p_x + ip_y) \end{bmatrix} & \boldsymbol{g}: \left| \frac{1}{2}, \frac{1}{2} \right\rangle - \left| \frac{1}{2}, -\frac{1}{2} \right\rangle &\propto \begin{bmatrix} -\sqrt{1/3}p_z \\ -\sqrt{1/3}(p_x + ip_y) \end{bmatrix} - \begin{bmatrix} -\sqrt{1/3}p_z \\ -\sqrt{1/3}(p_x + ip_y) \end{bmatrix} = \begin{bmatrix} -\sqrt{1/3}\pi_z^* \\ -\sqrt{1/3}(\sigma_x + i\pi_y^*) \end{bmatrix} \\
 \left| \frac{1}{2}, -\frac{1}{2} \right\rangle &\propto \begin{bmatrix} \sqrt{1/3}(p_x - ip_y) \\ -\sqrt{1/3}p_z \end{bmatrix} & \boldsymbol{u}: \left| \frac{1}{2}, \frac{1}{2} \right\rangle + \left| \frac{1}{2}, -\frac{1}{2} \right\rangle &\propto \begin{bmatrix} -\sqrt{1/3}p_z \\ -\sqrt{1/3}(p_x + ip_y) \end{bmatrix} + \begin{bmatrix} -\sqrt{1/3}p_z \\ -\sqrt{1/3}(p_x + ip_y) \end{bmatrix} = \begin{bmatrix} -\sqrt{1/3}\pi_x \\ -\sqrt{1/3}(\sigma_x^* + i\pi_y) \end{bmatrix} \\
 \left| \frac{3}{2}, +\frac{3}{2} \right\rangle &\propto \begin{bmatrix} \sqrt{1/2}(p_x + ip_y) \\ 0 \end{bmatrix} & \boldsymbol{g}: \left| \frac{3}{2}, \frac{3}{2} \right\rangle - \left| \frac{3}{2}, \frac{1}{2} \right\rangle &\propto \begin{bmatrix} \sqrt{1/2}(p_x + ip_y) \\ 0 \end{bmatrix} - \begin{bmatrix} \sqrt{1/2}(p_x + ip_y) \\ 0 \end{bmatrix} = \begin{bmatrix} -\sqrt{1/2}(\sigma_x + i\pi_y^*) \\ 0 \end{bmatrix} \\
 \left| \frac{3}{2}, -\frac{3}{2} \right\rangle &\propto \begin{bmatrix} 0 \\ \sqrt{1/2}(p_x - ip_y) \end{bmatrix} & \boldsymbol{u}: \left| \frac{3}{2}, \frac{3}{2} \right\rangle + \left| \frac{3}{2}, \frac{1}{2} \right\rangle &\propto \begin{bmatrix} \sqrt{1/2}(p_x + ip_y) \\ 0 \end{bmatrix} + \begin{bmatrix} \sqrt{1/2}(p_x + ip_y) \\ 0 \end{bmatrix} = \begin{bmatrix} -\sqrt{1/2}(\sigma_x^* + i\pi_y) \\ 0 \end{bmatrix} \\
 \left| \frac{3}{2}, +\frac{1}{2} \right\rangle &\propto \begin{bmatrix} \sqrt{3/2}p_z \\ -\sqrt{1/6}(p_x + ip_y) \end{bmatrix} & \boldsymbol{g}: \left| \frac{3}{2}, \frac{1}{2} \right\rangle - \left| \frac{3}{2}, -\frac{1}{2} \right\rangle &\propto \begin{bmatrix} \sqrt{3/2}p_z \\ -\sqrt{1/6}(p_x + ip_y) \end{bmatrix} - \begin{bmatrix} \sqrt{3/2}p_z \\ -\sqrt{1/6}(p_x + ip_y) \end{bmatrix} = \begin{bmatrix} -\sqrt{3/2}\pi_z^* \\ -\sqrt{1/6}(\sigma_x + i\pi_y^*) \end{bmatrix} \\
 \left| \frac{3}{2}, -\frac{1}{2} \right\rangle &\propto \begin{bmatrix} -\sqrt{1/6}(p_x + ip_y) \\ -\sqrt{3/2}p_z \end{bmatrix} & \boldsymbol{u}: \left| \frac{3}{2}, \frac{1}{2} \right\rangle + \left| \frac{3}{2}, -\frac{1}{2} \right\rangle &\propto \begin{bmatrix} \sqrt{3/2}p_z \\ -\sqrt{1/6}(p_x + ip_y) \end{bmatrix} + \begin{bmatrix} \sqrt{3/2}p_z \\ -\sqrt{1/6}(p_x + ip_y) \end{bmatrix} = \begin{bmatrix} -\sqrt{3/2}\pi_x \\ -\sqrt{1/6}(\sigma_x^* + i\pi_y) \end{bmatrix}
 \end{aligned}$$

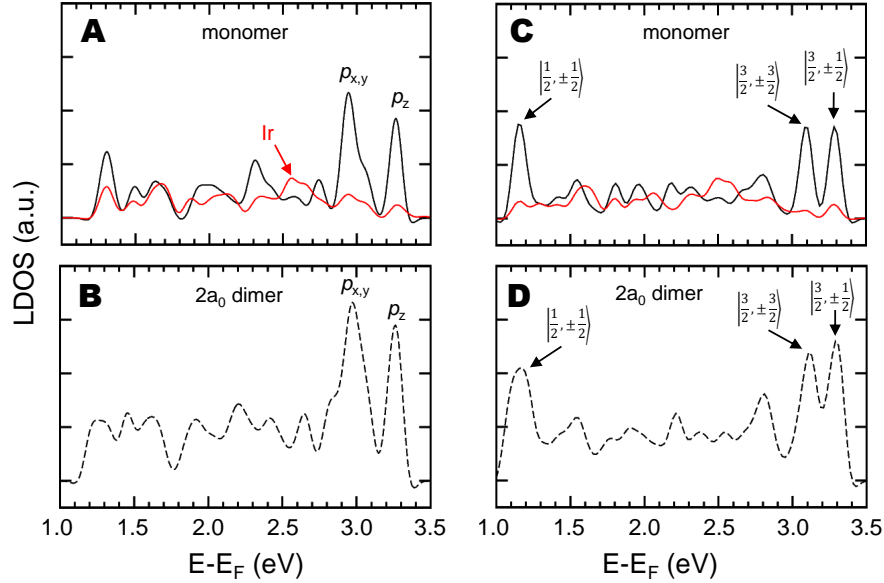
Supplementary Fig. 9: **Orbital characters of the Pb dimers on IrTe₂-(5×5) with/without spin-orbit coupling.** **a** without spin-orbit coupling, and **b** with spin-orbit coupling. The circles denote the angular momentum distribution (p_x : green, p_y : blue, and p_z : red) and its size is proportional to the localized state at Pb atom.



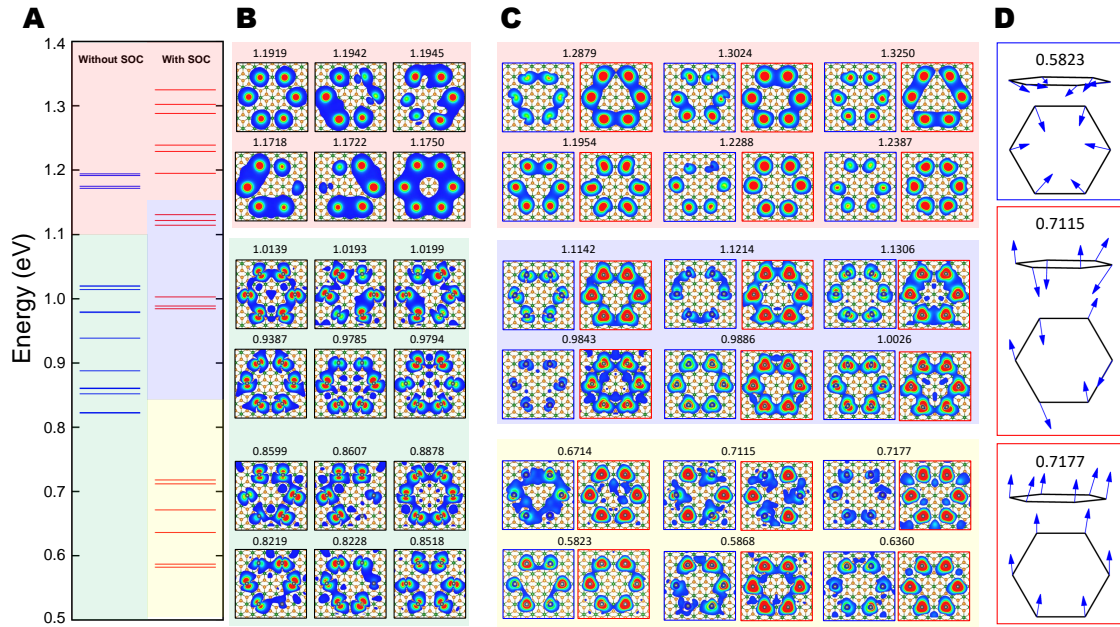
Supplementary Fig. 10: **Dipole interaction and spin-orbit coupling effect.** **a** Total charge difference ($\Delta\rho$), $\Delta\rho = \rho_{Pb/IrTe_2} - \rho_{IrTe_2} - \rho_{Pb-atom}$. Upper and down panel are without and with spin-orbit coupling, respectively. **b** Total charge difference of Pb on IrTe₂ between without and with spin-orbit coupling. $\Delta\rho = \rho_{Pb/IrTe_2(SOC)} - \rho_{Pb/IrTe_2}$. **c** In-plane summation of the charge difference. **e** Adsorption energy difference of Pb on IrTe₂ between without and with spin-orbit coupling. Dashed line denotes the fitting line with proportional to the 1 of r^3 . **f** Relative adsorption energy of the Pb molecules including the building block with the $\sqrt{3}a_0$ spacing.



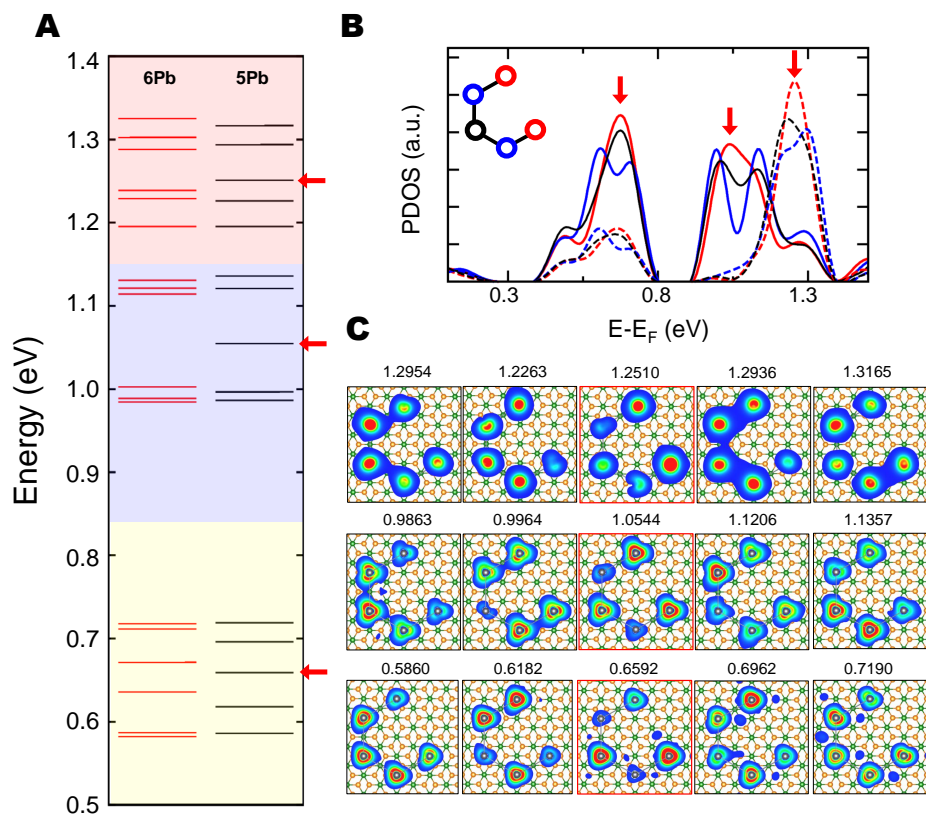
Supplementary Fig. 11: **Sn monomer and $2a_0$ dimer on IrTe_2 .** **a** and **b** are without spin-orbit coupling and **c** and **d** are with spin-orbit coupling. The Fermi level sets to zero.



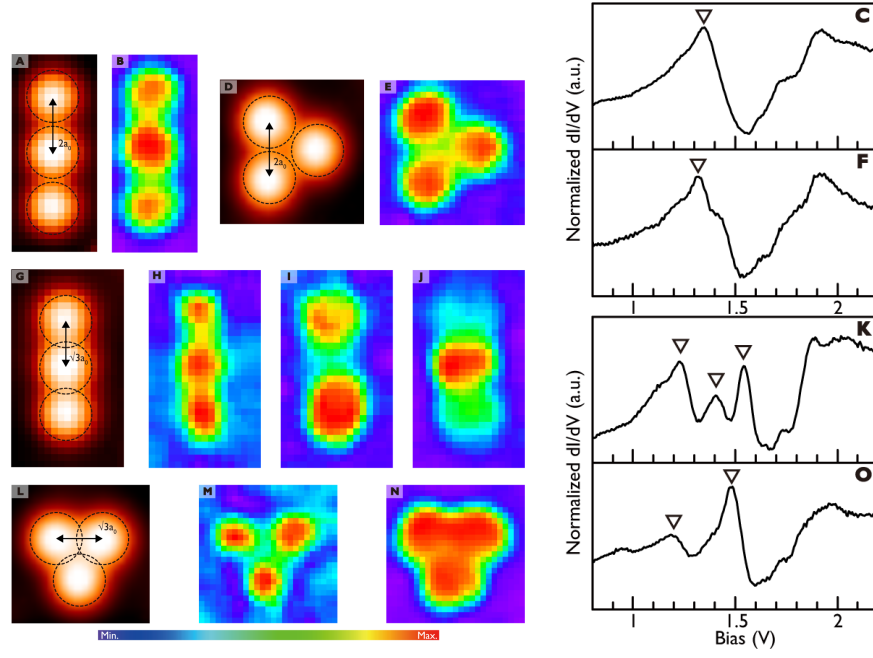
Supplementary Fig. 12: **Tl monomer and $2a_0$ dimer on IrTe_2 .** **a** and **b** are without spin-orbit coupling and **c** and **d** are with spin-orbit coupling. The red lines in **a** and **c** denote the localized states at Ir atom under the adsorbed Pb atom. The Fermi level sets to zero.



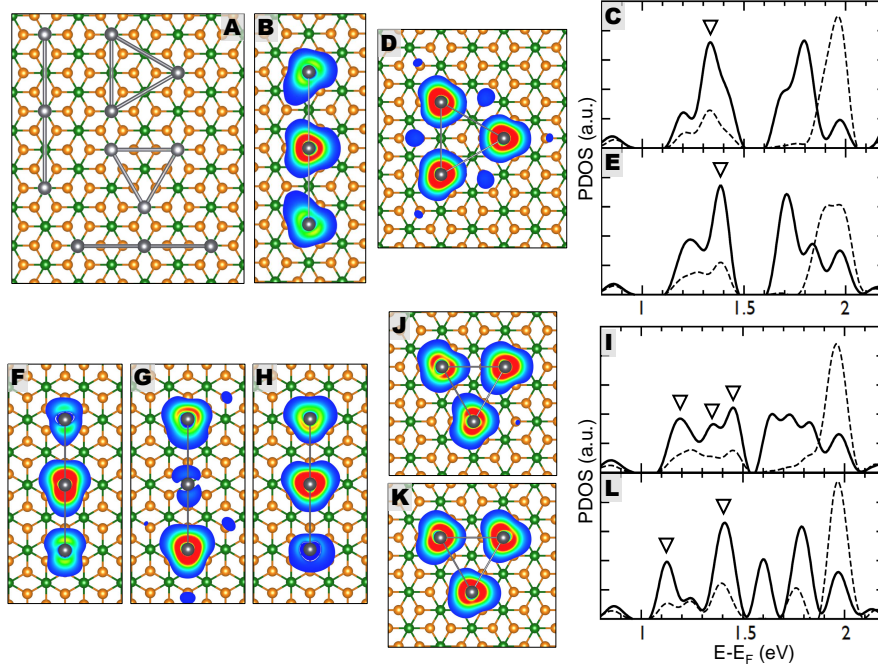
Supplementary Fig. 13: **Energy level and charge characters of the benzene-like Pb molecule on IrTe₂-(7×7) with/without spin-orbit coupling.** The Fermi level sets to zero. **a** The Γ point energy level for the $6p$ states of the Pb atom. **b** Charge characters without spin-orbit coupling. **c** Charge characters with spin-orbit coupling. For the case of spin-orbit coupling, there are two energetically degenerated states (red and blue) but distinguishable in their spin configuration. The number denote the corresponding energy level. **d** Selected spin configurations of rotational, anti-parallel and parallel in the $p_{1/2}$ states.



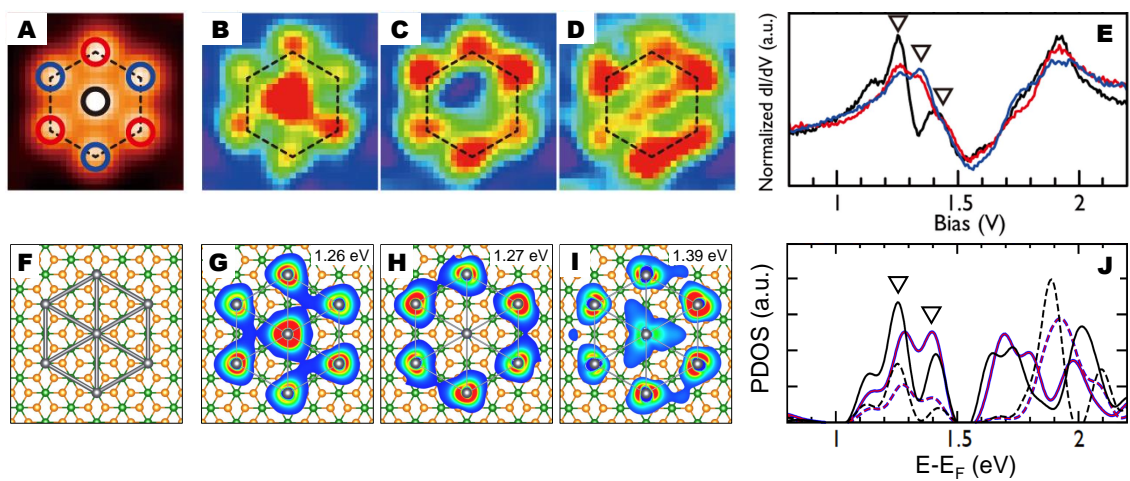
Supplementary Fig. 14: **Energy level and charge characters of the Pb pentamer on IrTe₂-(7×7).** **a** The Γ point energy level for the $6p$ states of the Pb atom. **b** Projected density of states. **c** Charge characters. The arrows indicate the edge states of three relativistic orbitals. The Fermi level sets to zero.



Supplementary Fig. 15: **Topography, dI/dV maps, and STS spectra of linear and triangular types of Pb trimers.** **a-c** Linear type with $2a_0$ spacing, **d-f** triangular type with $2a_0$ spacing, **g-k** linear type with $\sqrt{3}a_0$ spacing, and **l-o** triangular type with $\sqrt{3}a_0$ spacing.



Supplementary Fig. 16: **Charge characters and PDOS of the Pb trimers on IrTe_2 - (7×7) with spin-orbit coupling interaction.** **a** Atomic structures. **b-c** Linear type with $2a_0$ spacing, **d-e** triangular type with $2a_0$ spacing, **f-i** linear type with $\sqrt{3}a_0$ spacing, and **j-l** triangular type with $\sqrt{3}a_0$ spacing.



Supplementary Fig. 17: **The Pb heptamer on IrTe₂.** **a-e** Topography, dI/dV maps, and STS spectra. **f-j** Atomic structure, charge characters, and projected DOS.

Supplementary References

- [1] Kim, K. *et al.* Origin of first-order-type electronic and structural transition in IrTe₂, *Phys. Rev. Lett.* **114**, 136401 (2015).
- [2] Kim, H. S. *et al.* Nanoscale superconducting honeycomb charge order in IrTe₂, *Nano Lett.* **16**, 4260 (2016).